

Role of effective mass anisotropy in realizing a hybrid nodal-line fermion state


Bikash Patra ¹, Rahul Verma,¹ Shin-Ming Huang ^{2,3,4} and Bahadur Singh ^{1,*}

¹Department of Condensed Matter Physics and Materials Science, Tata Institute of Fundamental Research, Mumbai 400005, India

²Department of Physics, National Sun Yat-sen University, Kaohsiung 80424, Taiwan

³Center for Theoretical and Computational Physics, National Sun Yat-sen University, Kaohsiung 80424, Taiwan

⁴Physics Division, National Center for Theoretical Sciences, Taipei 10617, Taiwan

 (Received 1 June 2023; revised 9 October 2023; accepted 17 November 2023; published 12 December 2023)

Understanding the role of lattice geometry in shaping topological states and their properties is of fundamental importance to condensed matter and device physics. Here, we demonstrate how an anisotropic crystal lattice drives a topological hybrid nodal line in transition metal tetraphosphides MP_4 (M = transition metal). MP_4 constitutes a unique class of black phosphorus materials formed by intercalating transition metal ions between the phosphorus layers without destroying the characteristic anisotropic band structure of the black phosphorous. Based on the first-principles calculations and $k \cdot p$ theory, we show that MP_4 harbors a single hybrid nodal line formed between anisotropic Md and P states with oppositely oriented effective masses. The nodal line consists of both type-I and type-II nodal band crossings whose nature and location are determined by the effective mass anisotropies of the intersecting bands. We further discuss a possible topological phase transition to exemplify the formation of the hybrid nodal-line state in MP_4 . Our results offer a comprehensive study for understanding the interplay between structural motifs-driven mass anisotropies and topology in anisotropic lattice materials to realize hybrid semimetal states.

DOI: [10.1103/PhysRevB.108.235136](https://doi.org/10.1103/PhysRevB.108.235136)

I. INTRODUCTION

Since the discovery of topological insulators, the topology of electronic states and finding robust topological materials have attracted broad interest [1–4]. The initial topological state characterization based on free-fermion symmetries such as time reversal was generalized later to include topological states protected by crystalline symmetries [5–8]. In this way, many topological crystalline states such as mirror, inversion, and rotational Chern insulators and topological semimetals with Dirac, Weyl, nodal-line, nodal-chain, and higher-fold chiral fermions, among other possibilities, were proposed with their unique sets of nontrivial states and electromagnetic properties [2–9]. The topological states in materials are described uniquely by topological invariants that depend only on the symmetries of their underlying atomic positions [10–13]. Such topological state characterization has allowed unique symmetry-to-topology mapping that facilitated the identification of topological states in high-throughput materials searches, revealing many topological materials with unique nontrivial states [14–16]. These topological searches often neglect the effects of the spatial arrangement of atoms and their wave function properties even though they are essential for describing the numbers, energy-momentum relations, and geometries of the nontrivial states [17–19].

Among various topological states, topological nodal-line semimetals are considered parent phases for realizing

many exotic topological gapped or ungapped states through systematic lowering of crystalline symmetries [20–24]. They form one-dimensional (1D) valence and conduction band crossings in momentum space which realize new quasiparticles beyond the well-known Dirac, Weyl, and Majorana particles in high-energy physics. Analogous to Dirac and Weyl point semimetals, topological nodal-line semimetals can be classified as type-I, type-II, or hybrid nodal-line semimetals depending on the fermiology of the crossings bands [25–29]. In the type-I case, a nodal line is formed between electronlike and holelike bands and respects Lorentz symmetry. In type-II semimetals, the nodal line is formed between two electronlike or holelike bands, strongly breaking the Lorentz symmetry. In contrast, the hybrid nodal line consists of both the type-I and type-II band degeneracies that are naturally expected to occur if one of the crossing bands has a saddlelike energy dispersion. Such band crossings constitute a Fermi surface with electron and hole pockets that touch along specific directions in k space. The hybrid nodal line can realize amplified electron-correlation effects owing to the saddlelike energy dispersion and directional-dependent magnetotransport properties due to the Klein tunneling between the electron and hole pockets, among other phenomena [20,28–30].

Because the hybrid nodal lines constitute both the type-I and type-II band crossings located along different momentum space directions, their experimental realization remains a daunting challenge. Here, we propose that effective masses of the intersecting bands in anisotropic lattice materials can determine the dispersion and location of the nodal band crossings. Of importance is orthorhombic black phosphorus in

*Corresponding author: bahadur.singh@tifr.res.in

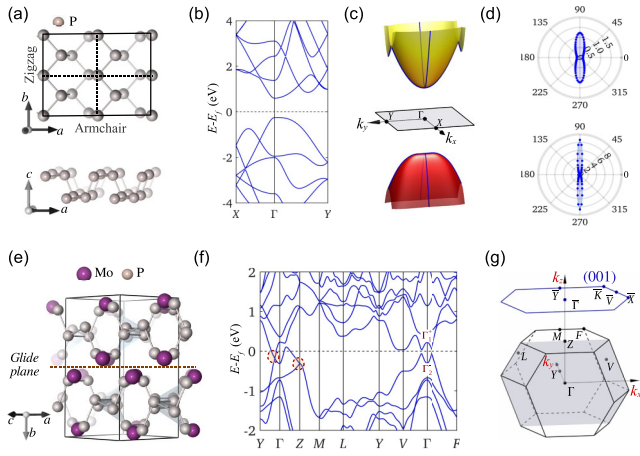


FIG. 1. Crystal lattice and electronic structure of phosphorene and MoP_4 . (a) Puckered honeycomb structure of a single phosphorene layer with distinct P-P bonding arrangements along the armchair (x axis) and zigzag (y axis) directions. The in-plane bonding anisotropy is the origin of the directional selective properties of phosphorene. Band structure of a single phosphorene layer (b) along the high-symmetry directions and (c) in the full two-dimensional Brillouin zone. (d) Calculated electron (top) and hole (bottom) carrier effective masses (in units of the mass of electrons m_e) of a single phosphorene layer in polar coordinates. $\theta = 0^\circ$ and $\theta = 90^\circ$ mark the armchair and zigzag directions, as shown in (a). (e) Perspective view of the bulk crystal lattice of MoP_4 with $C2/c$ (No. 15) symmetry. The dashed horizontal line marks the glide mirror plane. (f) First-principles semimetallic band structure of MoP_4 without spin-orbit coupling. Irreducible representations at the Γ point are marked. The symmetry-protected band crossings near the Fermi level are highlighted by dashed red circles. (g) The primitive cell Brillouin zone of MoP_4 with high-symmetry points. The mirror plane is in highlighted gray, and the projected (001) surface Brillouin zone is shown in blue.

which individual two-dimensional (2D) phosphorene layers are stacked together by weak van der Waals interactions [31–35]. Inside each phosphorene layer, the phosphorus atoms form a puckered honeycomb arrangement along the armchair direction and a bilayer configuration in the zigzag direction [see Figs. 1(a)–1(d)]. This unique structural motif drives the anisotropic electronic structure and physical properties that facilitate the use of black phosphorus in devices with directional selectivity [31–34]. The electronic structure and physical properties of black phosphorus can be engineered by pressure, doping, adsorption, and electric-field controls to realize an insulator-to-metal transition, topological semimetals with anisotropic Dirac bands, and superconductivity without destroying their anisotropic character [36–40]. Importantly, the intercalation of transition metal atoms in black phosphorus generates various low-symmetry transition metal tetraphosphides MP_4 (M = transition metal) that preserve the anisotropic electronic bands of black phosphorus, but with a semimetallic ground state [41–47]. Here, we show that MP_4 realizes a single hybrid nodal line driven by mass anisotropies of Md and P bands. By carefully exploring the structure-property-topology mapping in MP_4 , our results demonstrate how an anisotropic crystal structure shapes the low-energy topological states in materials.

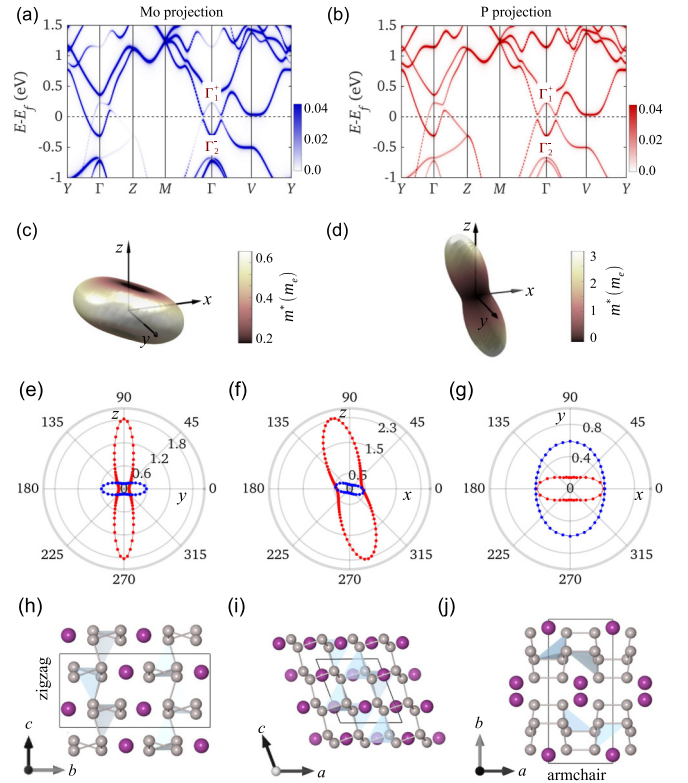


FIG. 2. Effective-mass anisotropy in MoP_4 . (a) Mo and (b) P atoms' resolved band structures of MoP_4 . The atomic weights are encoded in the color scale. An electron-type Mo band (Γ_2^-) intersects the P resolved valence band (Γ_1^+) near the Γ point. Calculated effective mass ellipsoid of (c) Mo and (d) P bands around the Γ point. A highly anisotropic peanut-shaped variation of the effective mass revealed the anisotropic character of P bands. (e)–(g) Calculated effective masses at constant planes for the Mo band (blue) and P band (red). The angular direction is given from the horizontal axis in each panel. (h)–(j) Two-dimensional view of the MoP_4 crystal structure in the b - c , a - c , and a - b planes. The zigzag and armchair directions are along the c and a directions, respectively. The P atomic layers are stacked along the b direction. The effective mass of the P band is much larger in the zigzag direction than in the armchair direction and follows the characteristic anisotropic structure of phosphorene.

II. METHODS

Electronic structure calculations were performed within the density functional theory framework with the projector augmented wave [48,49] potentials as implemented in the Vienna Ab initio Simulation Package (VASP) [50,51]. We used the Perdew-Burke-Ernzerhof parameterized generalized gradient approximation (GGA) [52] and hybrid Heyd-Scuseria-Ernzerhof (HSE) functionals for the exchange-correlation effects. The spin-orbit coupling (SOC) was included self-consistently to incorporate relativistic effects in the calculations. An energy cutoff of 400 eV for the plane wave basis set and an $8 \times 8 \times 10$ Γ -centered k mesh for the Brillouin zone sampling were used. Experimental lattice parameters with fully relaxed atomic positions were adopted to calculate the electronic structure and topological properties of MP_4 . We constructed a material-specific tight-binding model Hamiltonian from the atom-centered Wannier functions [53]. Md and

P *s* and *p* orbitals were used to construct the Wannier functions. The topological property and surface state calculations were performed using the WANNIERTOOLS package [54].

III. RESULTS

A. Crystal structure and anisotropic electronic properties

The anisotropic properties of black phosphorus stem in the anisotropic lattice of phosphorene, which is a 2D building block of black phosphorus [31–34]. The P atoms in phosphorene are covalently bonded with their three neighboring P atoms to form two in-plane and one out-of-plane bond, generating a hexagonal puckered lattice [Fig. 1(a)]. This atomic arrangement drives a highly anisotropic energy dispersion such that the conduction and valence bands are nearly flat along the zigzag direction (Γ –*Y*) and significantly dispersive along the armchair direction (Γ –*X*) near the band extremum point [see Figs. 1(b) and 1(c)]. Based on the energy dispersion, $E = \frac{\hbar^2 k^2}{2m^*}$, where m^* is the effective mass, we calculate the direction-dependent m^* and show the results in Fig 1(d). The effective masses are higher along the zigzag direction than the armchair direction for both the valence (hole) and conduction (electron) bands. The hole-effective masses are $8.62m_e$ and $0.14m_e$ (m_e is the mass of an electron in vacuum) along the zigzag and armchair directions, which yields a mass anisotropy of ~ 60 . Band crossings in such anisotropic bands can realize hybrid nodal dispersion under appropriate material parameters and symmetries, as discussed below.

Using phosphorene anisotropic band structure as a guideline, we searched among the black phosphorus materials and identified the most robust and ideal hybrid nodal-line candidate among the transition metal tetraphosphides MP_4 [41,44,45]. We discuss the structural and electronic properties of MP_4 by taking MoP_4 as an exemplary system. Single crystals of MoP_4 with a black-phosphorus-derived structure have been grown, and transport experiments have reported it as a semimetal with large positive magnetoresistance [44,45]. MoP_4 crystallizes in the monoclinic Bravais lattice with space group $C2/c$ (No. 15), which has lower symmetry than orthorhombic black phosphorus with $Cmce$ (No. 64). The experimental structural parameters are $a = 5.3131 \text{ \AA}$, $b = 11.1588 \text{ \AA}$, $c = 5.8343 \text{ \AA}$, and $\beta = 110.638^\circ$ [45]. The crystal structure is derived by intercalation of the Mo atoms between the phosphorene layers, which reorders the atomic stacking of phosphorene layers from AB to AC in a way similar to alkali metal intercalation in black phosphorus [42,43]. Figure 1(e) depicts the unit cell of MoP_4 . It consists of two phosphorene layers with Mo atoms sandwiched between them. The sandwiched Mo atoms form zigzag chains extending along [001] with a uniform interatomic distance of 3.20 \AA . There are 4 Mo and 16 P atoms in the unit cell. All the P atoms can be divided into two types. The first type of P atoms is covalently bonded with three adjacent P atoms and forms a dipolar bond with one Mo atom. The other type of P atoms is covalently bonded with two neighboring P atoms and forms dipolar bonds with two Mo atoms. This bonding arrangement distorts the P atoms from their original in-plane positions of black phosphorus and imposes three-dimensionality in MoP_4 . The crystal lattice respects only the following symmetries: inversion

TABLE I. Calculated effective masses of the P (Γ_1^+) and Mo (Γ_2^-) bands in the *y*–*z*, *x*–*z*, and *x*–*y* planes. The anisotropic ratio $\delta_{(\Gamma_1^+, \Gamma_2^-)} = \frac{m_{\max}^*}{m_{\min}^*}$, where m_{\max}^* and m_{\min}^* are the maximum and minimum effective masses in each plane for P and Mo bands, is also given. The angular location of m_{\max}^* and m_{\min}^* given in parentheses is calculated with respect to the horizontal axis in each plane (see Fig. 2). Effective masses are given in units of m_e .

Plane	P band (Γ_1^+)			Mo band (Γ_2^-)		
	m_{\max}^*	m_{\min}^*	$\delta_{\Gamma_1^+}$	m_{\max}^*	m_{\min}^*	$\delta_{\Gamma_2^-}$
<i>y</i> – <i>z</i>	1.82 (90°)	0.13 (0°)	14	0.59 (0°)	0.14 (90°)	4.21
<i>x</i> – <i>z</i>	2.34 (105°)	0.40 (15°)	5.85	0.47 (165°)	0.13 (75°)	3.61
<i>x</i> – <i>y</i>	0.42 (0°)	0.14 (90°)	3	0.59 (90°)	0.43 (0°)	1.37

\mathcal{I} , twofold rotation $\tilde{C}_{2y} : (x, y, z) \implies (-x, y, -z + \frac{1}{2})$, and a single glide mirror $\tilde{M}_y : (x, y, z) \implies (x, -y, z + \frac{1}{2})$. Figure 1(g) shows the primitive cell Brillouin zone (BZ) and projected (001) surface BZ with a marked \tilde{M}_y mirror plane and high-symmetry points.

Figure 1(f) shows the calculated band structure of MoP_4 without SOC. It is semimetallic where the Γ_1^+ valence band intersects the Γ_2^- conduction band with an inverted band ordering at the Γ point. Particularly, the valence and conduction band crossings stay ungapped along the Γ –*Y* direction. There are additional twofold band crossings along the *Z*–*M* direction in the valence and conduction regions of the band structure. Upon the inclusion of SOC, the band structure is locally gapped at each *k* point, separating valence and conduction bands in the entire BZ (see the Supplemental Material [55]). Nevertheless, the SOC-induced gap at the nodal points is less than 15 meV, which is slightly increased to a value of 25 meV when SOC is artificially scaled to 500%. The small band gap opening preserves the fermionology of the crossing bands, and thus, the SOC effects can be ignored. Moreover, the band crossings at the *Z* and *M* points in the valence and conduction regions remain robust, realizing nonsymmorphic symmetry-protected Dirac states in MoP_4 [45].

To uncover lattice-driven anisotropic electronic properties and their connection to black phosphorus, we present the orbital-resolved band structure of MoP_4 in Figs. 2(a) and 2(b). The conduction band is derived from the Mo atoms, whereas the valence band is composed of P atoms. These two bands with distinct atomic character cross in the vicinity of the Fermi level to generate a semimetallic state. The nature of the valence and conduction bands is further probed by calculating the orientation-dependent effective masses around the Γ point (see Table I). In Figs. 2(c) and 2(d), we present these results for the Mo and P bands, respectively, in the *x*–*y*–*z* space. The effective mass associated with the Mo band is less anisotropic and forms a spheroid shape in space, whereas the P band effective mass is highly anisotropic, forming a peanutlike shape and mimicking the anisotropic P lattice structure in MoP_4 . The structure-to-mass-anisotropy relation is revealed by the results shown on various plane cuts in Figs. 2(e)–2(g) and their associated crystal directions in Figs. 2(h)–2(j). Particularly, the P band effective mass (red markers) along the

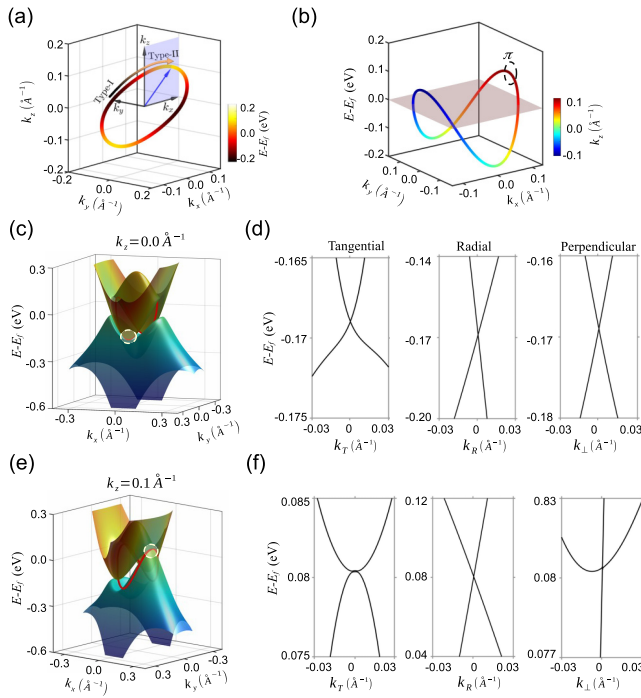


FIG. 3. Hybrid nodal line in MoP₄. (a) The location of the nodal line in the reciprocal space. The color represents the nodal-line energy. The arrow shows the transition from type-I to type-II points. The upper and lower portions of the nodal line across Γ are related by inversion symmetry. (b) Energy-dependent nodal-line configuration on the k_x - k_y plane. An extended energy region below and above the Fermi level (shown by the gray plane) is revealed. The color represents the k_z location of the nodal line. (c) and (e) Band structure in the k_x - k_y plane at (c) $k_z = 0 \text{ \AA}^{-1}$ and (e) $k_z = 0.1 \text{ \AA}^{-1}$ with the nodal line (red line). (d) and (f) Energy dispersion along the tangential, radial, and perpendicular directions around the shaded points in (c) and (e). At any point on the nodal line, k_R defines the radial direction, k_T lies perpendicular to k_R in the nodal-line plane, and k_\perp lies normal to the nodal-line plane. From these energy dispersion cuts a type-I character at $k_z = 0 \text{ \AA}^{-1}$ and a type-II character (that is, along perpendicular directions both the crossing bands have the same sign for velocity) at $k_z = 0.1 \text{ \AA}^{-1}$ are revealed.

zigzag direction is higher than that in the armchair direction, similar to phosphorene bands. In contrast, the Mo bands (blue markers) exhibit maximum and minimum effective masses oriented perpendicular to the P bands. The Mo and P bands with oppositely oriented effective masses cross in the vicinity of the Fermi level to generate a semimetallic state.

B. Hybrid nodal-line structure

We now characterize the band crossings between Mo and P bands in Fig. 3. The gapless valence and conduction band crossing points in k_x - k_y - k_z space are presented in Fig. 3(a). These crossing points trace a line node that encloses the Γ point. The line node is not hooked to the k_y mirror plane but forms an \mathcal{IT} symmetric structure primarily located on the k_x - k_z plane due to the presence of inversion symmetry. The symmetry protection of the nodal line is determined by calculating the Berry phase $\gamma = \oint dk \cdot A(k)$, where

$A(k) = i \sum_n \langle u_{n,k} | \nabla u_{n,k} \rangle$ is the Berry connection of the occupied Bloch bands $|u_{n,k}\rangle$. For a generic closed k loop encircling the line node, we obtain a Berry phase $\gamma = +\pi$. This results in a nontrivial winding number $\frac{\gamma}{\pi} = +1$, dictating the topological protection of the line node. The energy and momentum spread of the line node are shown in Figs. 3(a) and 3(b). The line node spans an energy range from -0.17 to 0.08 eV that passes through the Fermi level. Such an extended energy range can enable spectroscopic verifications of the nodal line without fine-tuning the Fermi level in MoP₄.

Figures 3(c) and 3(e) show the E - k_x - k_y band dispersion in the $k_z = 0$ and $k_z = 0.1 \text{ \AA}^{-1}$ planes, respectively, with the line node shown in red. The isolated nodal points (shaded white circle) lie on the k_y axis in the $k_z = 0$ plane and on the k_x axis in the $k_z = 0.1$ plane. We further plot the energy dispersion away from these nodal points in Figs. 3(d) and 3(f). Dispersing away from the nodal points, the two bands form a nearly quadratic band crossing along the tangential direction and conical band crossings along the other two momentum directions on the $k_z = 0$ plane. In contrast, the two bands have the same sign for velocity along one momentum direction (in this case, the direction perpendicular to the nodal-line plane) on the $k_z = 0.1 \text{ \AA}^{-1}$ plane. These results clearly show that the line node is hybrid in character, having both type-I and type-II band crossings. Exploring the full momentum space location of type-I and type-II band crossings, we find that the type of band crossings is related to their lattice directions. In particular, the type-I nodal points lie along the armchair directions, whereas the type-II band touchings lie along the zigzag direction of the P atoms. The nodal-line dispersion continuously evolves from type I to type II in intermediate directions, as shown by an arrow in Fig. 3(a) (see the Supplemental Material [55] for details). Such a hybrid nodal structure arises due to crossings of anisotropic Mo and P bands with oppositely oriented effective masses, which generates a dispersive nodal line by displacing the crossing bands in opposite momentum directions. The large opposite displacement between the crossing bands drives type-II dispersion along certain momentum directions (see Sec. III D).

C. Topological surface states

The existence of drumhead electron states inside or outside nodal-line projections on the crystal surface is the hallmark of topological nodal-line semimetals. To showcase these states, we present the calculated (001) surface band structure of MoP₄ in Fig. 4. In Figs. 4(a) and 4(b), we illustrate the constant-energy contours at $E = -0.169$ eV and $E = 0.08$ eV as the representative cases of type-I and type-II bulk nodal energies, respectively. These plots show a rich electronic structure with surface states located inside and outside the projected nodal line. The surface states connect two nodal points at a particular energy cut, forming a double Fermi-arc-type connectivity. These Fermi-arc-type states are part of the highly dispersive drumhead surface states, as seen in the surface band structure along the \bar{Y} - Γ - \bar{Y} and \bar{X} - Γ - \bar{X} directions in Figs. 4(c) and 4(d). Such drumhead electronic states and their Fermi-arc-type constant-energy connectivity are unique to the dispersive hybrid line node and may serve as spectroscopic fingerprints for experimental verification.

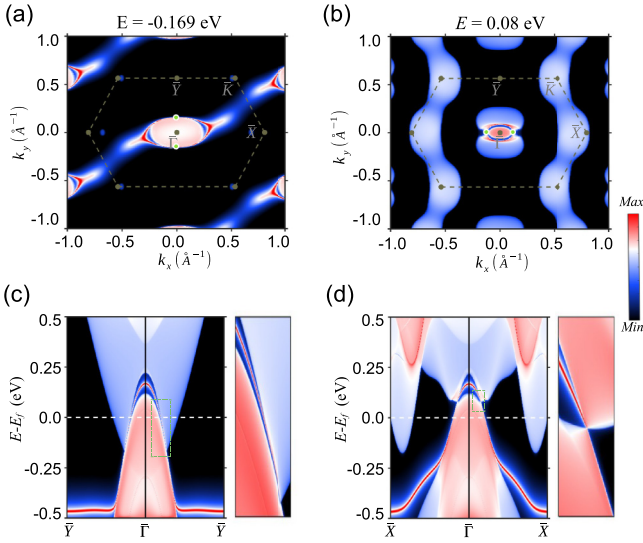


FIG. 4. Topological surface states in MoP₄. Surface energy spectrum for the (001) surface of MoP₄ at constant energies (a) $E = -0.169$ eV and (b) $E = 0.08$ eV obtained with a surface potential energy of -50 meV. The green dots in (a) and (b) mark the type-I and type-II projected band crossings along the high-symmetry axes, respectively. A Fermi-arc-type connectivity is revealed in the drumhead surface states at these isoenergy contours. Surface band structure of the (001) surface along the (c) $\bar{Y}-\bar{\Gamma}-\bar{Y}$ and (d) $\bar{X}-\bar{\Gamma}-\bar{X}$ directions. The left panel shows a close-up of the band structure highlighted in the dashed box. The drumhead surface states lie inside the projected bulk band crossings.

D. Effective Hamiltonian

To better understand the underlying mechanism of a mass-anisotropy-driven hybrid nodal line, we derive the low-energy effective Hamiltonian using the theory of invariants [19,56]. The first-principles results indicate that anisotropic Γ_2^- and Γ_1^+ bands cross to generate the hybrid nodal line. A $k \cdot p$ Hamiltonian around Γ is constrained by time-reversal symmetry $\Theta: H^*(\mathbf{k}) = H(-\mathbf{k})$, glide mirror symmetry $\tilde{M}_y: H(\mathbf{k}) = H(M_y \mathbf{k})$, and inversion symmetry $\mathcal{I}: \sigma_z H(\mathbf{k}) \sigma_z = H(-\mathbf{k})$, where σ_z is a Pauli matrix. Based on these symmetry constraints, the spinless two-band $k \cdot p$ Hamiltonian takes the form

$$H(\mathbf{k}) = \begin{pmatrix} \varepsilon^{(u)}(\mathbf{k}) & \Delta(\mathbf{k}) \\ \Delta^*(\mathbf{k}) & \varepsilon^{(l)}(\mathbf{k}) \end{pmatrix}, \quad (1)$$

where $\varepsilon^{(u)}$ and $\varepsilon^{(l)}$ are associated with Γ_2^- and Γ_1^+ bands with

$$\varepsilon^{(u,l)}(\mathbf{k}) = \pm \left\{ \sum_{i=x,y,z} \left(\frac{1}{2} \alpha_i^{(u,l)} k_i^2 \right) + \alpha_{xz}^{(u,l)} k_x k_z + \frac{1}{2} \varepsilon_0 \right\}, \quad (2)$$

$$\Delta(\mathbf{k}) = -iV(v_x k_x - v_z k_z). \quad (3)$$

Here, all the parameters are considered to be real. To have concave upward and downward curves for $\varepsilon^{(u)}$ and $\varepsilon^{(l)}$, the inverse of absolute effective masses $\alpha_i^{(u)}, \alpha_i^{(l)} > 0$ for $i = x, y, z$ (here, $\hbar = 1$). The $\alpha_{xz}^{(u,l)}$ term is introduced to break the mirror symmetry in the k_x and k_z planes, giving tilted effective mass eclipses, as found in our calculations. $\varepsilon_0 < 0$ gives the

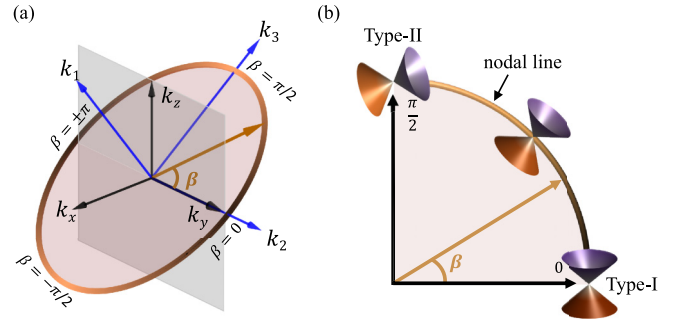


FIG. 5. Nodal-ring configuration and energy dispersion. (a) Nodal-ring configuration in the global coordinate system (k_x, k_y, k_z). A new coordinate system (k_1, k_2, k_3) is defined in which k_2 is along k_y , k_1 is perpendicular to the nodal-ring plane, and k_3 is perpendicular to k_1 and k_2 and lies in the nodal-ring plane. The nodal ring is parametrized by $\beta \in [-\pi, \pi]$. (b) Variation of nodal-ring energy dispersion as a function of β in the first quadrant. The energy dispersion evolves from type I to type II for $\beta = 0$ to $\beta = \pi/2$.

band inversion between the two bands at Γ . $\Delta(\mathbf{k})$ describes the interband coupling with strength $|\mathbf{V}\mathbf{k}|$. The dimensionless parameters v_x and v_z with the constraint $v_x^2 + v_z^2 = 1$ describe the anisotropy due to interband coupling. The eigenenergies associated with the Hamiltonian [Eq. (1)] are

$$E_{\pm}(\mathbf{k}) = \xi^{(+)}(\mathbf{k}) \pm \sqrt{\xi^{(-)}(\mathbf{k})^2 + |\Delta(\mathbf{k})|^2}, \quad (4)$$

where $\xi^{(\pm)}(\mathbf{k}) = \frac{1}{2}[\varepsilon^{(u)}(\mathbf{k}) \pm \varepsilon^{(l)}(\mathbf{k})]$. For later use, we define $\alpha_X^{(u,l)} = v_z^2 \alpha_x^{(u,l)} + v_x^2 \alpha_z^{(u,l)} + 2v_x v_z \alpha_{xz}^{(u,l)}$, and $\alpha_Z^{(u,l)} = v_x v_z (\alpha_x^{(u,l)} - \alpha_z^{(u,l)}) + (v_x^2 - v_z^2) \alpha_{xz}^{(u,l)}$.

Since the two crossing bands have equal mirror eigenvalues, their nodal crossings are not protected by \tilde{M}_y . Instead, the inversion symmetry \mathcal{I} can protect a line nodal, which is determined by the conditions $\xi^{(-)}(\mathbf{k}) = 0$ and $\Delta(\mathbf{k}) = 0$. The nodal ring for $\beta \in (-\pi, \pi]$ [see Fig. 5(b)] is positioned at

$$\mathbf{k}_{\text{node}}(\beta) = (v_z K_X \sin(\beta), \pm K_Y \cos(\beta), v_x K_X \sin(\beta)), \quad (5)$$

where $K_X = \sqrt{\frac{|\varepsilon_0|}{\alpha_x}}$ and $K_Y = \sqrt{\frac{|\varepsilon_0|}{\alpha_y}}$.

To describe the local energy dispersion associated with nodal crossings for different β , we define a new coordinate system (k_1, k_2, k_3), as shown in Fig. 5(a). The transformation of $(k_1, k_2, k_3) \rightarrow (k_x, k_y, k_z)$ is $k_x = v_x k_1 + v_z k_3$, $k_y = k_2$, and $k_z = -v_z k_1 + v_x k_3$. Here, k_1 is perpendicular to the nodal-ring plane [$\Delta(\mathbf{k}) = 0$]. Taking $k_2 = K_Y \cos(\beta)$ and $k_3 = K_X \sin(\beta)$ on the nodal ring, the dispersions of $\varepsilon^{(u)}$ and $\varepsilon^{(l)}$ along k_1 take the form

$$\varepsilon^{(u,l)}(k_1) = \pm \left\{ \frac{1}{2} A^{(u,l)} k_1^2 + \alpha_Z^{(u,l)} K_X \sin(\beta) k_1 \right\} + E_{\text{node}}(\beta), \quad (6)$$

where $A^{(u,l)} = \alpha_x^{(u,l)} + \alpha_z^{(u,l)} - \alpha_X^{(u,l)}$. $E_{\text{node}}(\beta) = \frac{1}{2} K_X^2 \delta \alpha_X \sin^2(\beta) + \frac{1}{2} K_Y^2 \delta \alpha_Y \cos^2(\beta)$ is the energy of the nodal ring, which agrees with our first-principles results [Fig. 3(b)] for $K_X^2 \delta \alpha_X > K_Y^2 \delta \alpha_Y$. The energy dispersions $\varepsilon^{(u,l)}(k_1)$ shows shifted parabolic bands that cross at $k_1 = 0$ with shifts proportional to $\alpha_Z^{(u,l)} \sin(\beta)$. Notably, the band shifts increase with β . When the band shifts are opposite, $\alpha_Z^{(u)} \alpha_Z^{(l)} < 0$, a

type-II feature emerges [Fig. 5(b)]. Below we show that this is the necessary condition for realizing a type-II band crossing.

Including the interband coupling, $\Delta(\mathbf{k}) = -iV k_1$, the slopes of $E_{\pm}(\mathbf{k})$ along k_1 are

$$\frac{\partial}{\partial k_1} E_{\pm}(\mathbf{k}) = K_X \delta\alpha_Z \sin(\beta) \pm \sqrt{[K_X \alpha_Z \sin(\beta)]^2 + V^2}, \quad (7)$$

where $\alpha_Z = \frac{1}{2}(\alpha_z^{(u)} + \alpha_z^{(l)})$ and $\delta\alpha_Z = \frac{1}{2}(\alpha_z^{(u)} - \alpha_z^{(l)})$. The condition for a type-II nodal dispersion is

$$|\delta\alpha_Z K_X \sin(\beta)| > \sqrt{[\alpha_Z K_X \sin(\beta)]^2 + V^2}, \quad (8)$$

which reduces to

$$(-\alpha_Z^{(u)} \alpha_Z^{(l)}) \sin^2(\beta) > \left(\frac{V}{K_X}\right)^2. \quad (9)$$

Notably, $\alpha_Z^{(u,l)}$ characterizes the dressed mass anisotropy in the k_x - k_z plane for the two bands. The necessary condition for realizing a type-II band dispersion is that the mass anisotropies of the crossing bands should be opposite, $\alpha_Z^{(u)} \alpha_Z^{(l)} < 0$. For small β and finite V , Eq. (9) cannot be satisfied. This can be understood because for $\beta = 0$, there is no k shift in Eq. (6), and the band crossing should be type I. However, when β approaches $\pm\pi/2$, a type-II band crossing can be realized [Fig. 5(b)] in the k_1 direction provided bands have large mass anisotropy: $|\beta| > \arcsin(|V|/K_X \sqrt{-\alpha_Z^{(u)} \alpha_Z^{(l)}})$. The dispersion along k_2 always remains type I, as found in our first-principles results.

We emphasize that Eq. (9) is the main result of our work. Taking $\sin^2(\beta) = 1$ describes the condition for a hybrid nodal ring. A large opposite mass anisotropy of the crossing bands is an ingredient for realizing a hybrid nodal line in materials. More precisely, the anisotropy includes the effect of particle-hole asymmetry between the bands. When the conduction and valence bands have opposite mass anisotropies like in MP_4 , the crossing bands form a hybrid nodal line.

E. Material tunability and phase transition

We now consider the robustness of the hybrid node line and demonstrate a semimetal-to-insulator transition in MP_4 . Owing to the presence of $M d$ bands, the electronic correlations may play an important role in dictating the nature of the nodal line in MP_4 since they could shape the energy dispersion and effective masses of the crossings bands. In Fig. 6(a), we present the band structure of MoP_4 obtained with the HSE06 hybrid functional that incorporates part of the exact Fock exchange [57]. The calculated energy dispersions of the valence and conduction bands remain preserved, although their band overlap is reduced compared to the GGA results. On exploring the mass anisotropies and nodal-line energy dispersion, we find that the hybrid nodal line is quite robust to the changes in the exchange-correlation functionals (see the Supplemental Material [55]). However, due to reduced overlap between the valence and conduction bands, MoP_4 lies close to a semimetal-to-insulator transition point.

In order to discuss the semimetal-to-insulator transition and the tunability of the hybrid nodal line, it is useful to

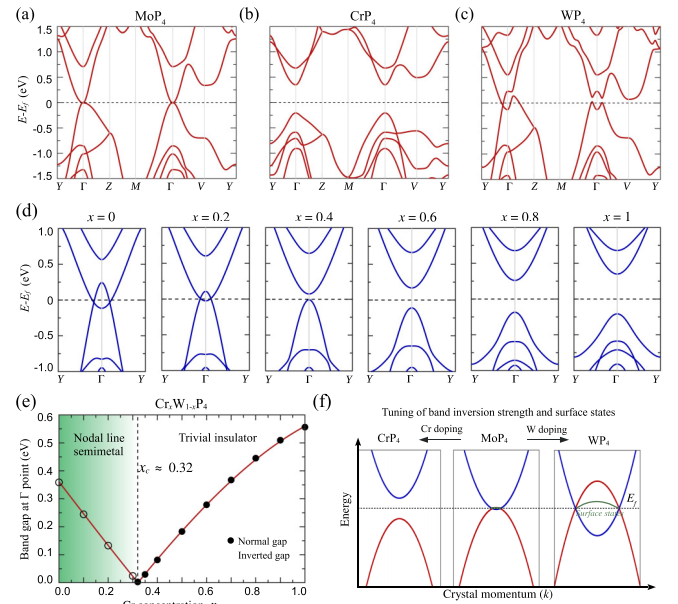


FIG. 6. Hybrid nodal-line-to-insulator transition and phase tunability. Band structures of (a) MoP_4 , (b) CrP_4 , and (c) WP_4 obtained using the HSE hybrid exchange-correlation functional. (d) Calculated band structure of $Cr_x W_{1-x} P_4$ along the $Y-\Gamma-Y$ direction for different x values. (e) Variation of the energy gap at Γ for $Cr_x W_{1-x} P_4$ as a function of x . The related topological state is highlighted. The red line is a guide to the eye. (f) Schematic representation of the calculated hybrid-functional band structure of representative compounds in the MP_4 family. Band inversion strength increases in WP_4 , whereas CrP_4 realizes a fully gapped state.

calculate the HSE06 band structures of CrP_4 and WP_4 [Figs. 6(b) and 6(c)]. Since CrP_4 and WP_4 are isostructural to MoP_4 , they show similar mass anisotropies in the valence and conduction bands, as seen in MoP_4 [44–46]. However, the magnitude of effective masses and anisotropy are material dependent owing to distinct interband coupling effects (see the Supplemental Material [55] for details). This can be further understood based on the different structural parameters of MP_4 . Due to the different effective radii of the M atoms, the lattice constant is decreased in CrP_4 ($a = 5.19 \text{ \AA}$, $b = 10.16 \text{ \AA}$, and $c = 5.77 \text{ \AA}$) and increased in WP_4 ($a = 5.34 \text{ \AA}$, $b = 11.19 \text{ \AA}$, and $c = 5.87 \text{ \AA}$) compared to MoP_4 . The change in lattice parameters results in different crystal-field effects and electronic states in CrP_4 and WP_4 . Particularly, CrP_4 realizes an insulator state with a band gap of 0.54 eV at the Γ point, whereas WP_4 forms a hybrid nodal line with increased band inversion strength. These results demonstrate that CrP_4 and WP_4 lie electronically on opposite sides of MoP_4 . Alternatively, Cr doping in MoP_4 will be expected to reduce the valence and conduction band overlap and push the material toward the trivial insulator state. In contrast, W doping in MoP_4 will increase the band overlap and realize a hybrid nodal line with increased band inversion strength.

Figure 6(d) shows energy dispersion of $Cr_x W_{1-x} P_4$ alloys for various Cr concentrations x calculated along the k_y axis. The virtual crystal approximation is adopted to model the band structure using the Wannier Hamiltonian obtained with the HSE06 functional. When $x = 0$, a clear overlap

between M d and P p states is seen, so the system realizes a nodal-line semimetal state. As x is increased, the M d and P p states move in opposite energy directions and touch at the Γ point for $x_c = 0.32$. With a further increase in x , the overlap between these states vanishes, and the system transitions to an insulator state. Notably, we calculate the orientation-dependent effective masses of the valence and conduction bands and the nodal-line dispersion of $\text{Cr}_x\text{W}_{1-x}\text{P}_4$ for $x = 0.2$. The mass anisotropy of bands and the hybrid nature of the nodal-line dispersion remain preserved, showing that these features are robust in MP_4 materials. The evolution of the band gap of $\text{Cr}_x\text{W}_{1-x}\text{P}_4$ as a function of x at Γ is shown in Fig. 6(e). A hybrid semimetal-to-insulator transition can thus be achieved by varying the Cr concentration. A similar tunable system can be achieved by doping MoP_4 with Cr atoms [see Fig. 6(f)]. Since Cr, W, and Mo atoms are isovalent and form isostructural materials with similar mass anisotropies, one can create a $\text{Cr}_x(\text{Mo}, \text{W})_{1-x}\text{P}_4$ material that can be tuned among various topological states.

IV. DISCUSSION

Understanding the structure-to-property relationship lies at the heart of physics research and provides concepts for engineering new device design [35]. It remains largely unexplored in topological materials, even though the numbers and energy dispersions of nontrivial states depend on the structural and positional motifs of materials. Based on the first-principles calculations and $k \cdot p$ theory, we have systematically demonstrated how the lattice-geometry-driven effective mass anisotropies result in unique hybrid nodal-line states in black phosphorus materials MP_4 . Taking MoP_4 as an explicit example, we showed that it retains characteristic anisotropic energy dispersion of the phosphorene and harbors a single hybrid nodal line between Mo d and P p states. The nodal line constitutes both type-I and type-II band crossings and spreads across the Fermi level around the Γ point. We revealed that the P bands have a peanut-type effective mass

variation such that the large and small effective masses orient along the zigzag and armchair directions of the P atoms, respectively. The anisotropic P band crosses with the Mo d band to form the hybrid nodal line where the type-I and type-II nodal points are hooked to the armchair and zigzag lattice directions. Through in-depth symmetry and Hamiltonian analysis, we showed that strong mass anisotropy in the crossing bands is a necessary condition to form the hybrid nodal line in MP_4 . We further proposed the realization of the hybrid nodal-line state with increased inversion strength and a metal-to-insulator transition through isoelectronic chemical substitutions such as $\text{Cr}_x(\text{W}, \text{Mo})_{1-x}\text{P}_4$. MP_4 materials have been synthesized in experiments and explored in connection with high diffusion anisotropy of sodium and other metal ions in the phosphorous layers [41–47]. More recent work discussed the high-pressure synthesis of MoP_4 and revealed its semimetallic nature with high-mobility electrons [45]. Since the single-crystalline samples have been grown and the hybrid nodal line runs across the Fermi level, experimental validation of the nodal line could be done, for example, in photoemission experiments without any Fermi level tuning. Moreover, orientation-dependent effective masses could be determined from transport experiments. Their anisotropic behavior could serve as experimental fingerprints to determine the nodal-line dispersion in topological semimetals. These facts highlight that MP_4 materials constitute an ideal platform to explore mass-anisotropy-driven hybrid nodal states and advance our understanding of the role of lattice geometry in shaping topological state dispersion in materials.

ACKNOWLEDGMENTS

This work is supported by the Department of Atomic Energy of the Government of India under Project No. 12-R&D-TFR-5.10-0100 and benefited from the computational resources of TIFR Mumbai. S.-M.H. is supported by the NSTC-AFOSR Taiwan program on Topological and Nanostructured Materials, Grant No. 110-2124-M-110-002-MY3.

B.P. and R.V. contributed equally to this work.

-
- [1] M. Z. Hasan and C. L. Kane, *Colloquium: Topological insulators*, *Rev. Mod. Phys.* **82**, 3045 (2010).
 - [2] A. Bansil, H. Lin, and T. Das, *Colloquium: Topological band theory*, *Rev. Mod. Phys.* **88**, 021004 (2016).
 - [3] N. P. Armitage, E. J. Mele, and A. Vishwanath, Weyl and Dirac semimetals in three-dimensional solids, *Rev. Mod. Phys.* **90**, 015001 (2018).
 - [4] B. Singh, H. Lin, and A. Bansil, Topology and symmetry in quantum materials, *Adv. Mater.* **35**, 2201058 (2022).
 - [5] L. Fu, Topological crystalline insulators, *Phys. Rev. Lett.* **106**, 106802 (2011).
 - [6] T. H. Hsieh, H. Lin, J. Liu, W. Duan, A. Bansil, and L. Fu, Topological crystalline insulators in the SnTe material class, *Nat. Commun.* **3**, 982 (2012).
 - [7] C. Fang and L. Fu, New classes of topological crystalline insulators having surface rotation anomaly, *Sci. Adv.* **5**, eaat2374 (2019).
 - [8] B. Bradlyn, J. Cano, Z. Wang, M. G. Vergniory, C. Felser, R. J. Cava, and B. A. Bernevig, Beyond Dirac and Weyl fermions: Unconventional quasiparticles in conventional crystals, *Science* **353**, aaf5037 (2016).
 - [9] D. Xiao, M.-C. Chang, and Q. Niu, Berry phase effects on electronic properties, *Rev. Mod. Phys.* **82**, 1959 (2010).
 - [10] R.-J. Slager, A. Mesaros, V. Juričić, and J. Zaanen, The space group classification of topological band-insulators, *Nat. Phys.* **9**, 98 (2013).
 - [11] J. Kruthoff, J. de Boer, J. van Wezel, C. L. Kane, and R.-J. Slager, Topological classification of crystalline insulators through band structure combinatorics, *Phys. Rev. X* **7**, 041069 (2017).
 - [12] B. Bradlyn, L. Elcoro, J. Cano, M. G. Vergniory, Z. Wang, C. Felser, M. I. Aroyo, and B. A. Bernevig, Topological quantum chemistry, *Nature (London)* **547**, 298 (2017).

- [13] Z. Song, T. Zhang, Z. Fang, and C. Fang, Quantitative mappings between symmetry and topology in solids, *Nat. Commun.* **9**, 3530 (2018).
- [14] T. Zhang, Y. Jiang, Z. Song, H. Huang, Y. He, Z. Fang, H. Weng, and C. Fang, Catalogue of topological electronic materials, *Nature (London)* **566**, 475 (2019).
- [15] M. G. Vergniory, L. Elcoro, C. Felser, N. Regnault, B. A. Bernevig, and Z. Wang, A complete catalogue of high-quality topological materials, *Nature (London)* **566**, 480 (2019).
- [16] F. Tang, H. C. Po, A. Vishwanath, and X. Wan, Comprehensive search for topological materials using symmetry indicators, *Nature (London)* **566**, 486 (2019).
- [17] H. Lin, T. Das, Y. Okada, M. C. Boyer, W. D. Wise, M. Tomasik, B. Zhen, E. W. Hudson, W. Zhou, V. Madhavan, C.-Y. Ren, H. Ikuta, and A. Bansil, Topological dangling bonds with large spin splitting and enhanced spin polarization on the surfaces of Bi_2Se_3 , *Nano Lett.* **13**, 1915 (2013).
- [18] B. Singh, H. Lin, R. Prasad, and A. Bansil, Role of surface termination in realizing well-isolated topological surface states within the bulk band gap in TlBiSe_2 and TlBiTe_2 , *Phys. Rev. B* **93**, 085113 (2016).
- [19] B. Singh, X. Zhou, H. Lin, and A. Bansil, Saddle-like topological surface states on the $TT'X$ family of compounds ($T, T' =$ Transition metal, $X = \text{Si, Ge}$), *Phys. Rev. B* **97**, 075125 (2018).
- [20] A. A. Burkov, M. D. Hook, and L. Balents, Topological nodal semimetals, *Phys. Rev. B* **84**, 235126 (2011).
- [21] C. Fang, Y. Chen, H.-Y. Kee, and L. Fu, Topological nodal line semimetals with and without spin-orbital coupling, *Phys. Rev. B* **92**, 081201(R) (2015).
- [22] G. Bian, T.-R. Chang, H. Zheng, S. Velury, S.-Y. Xu, T. Neupert, C.-K. Chiu, S.-M. Huang, D. S. Sanchez, I. Belopolski, N. Alidoust, P.-J. Chen, G. Chang, A. Bansil, H.-T. Jeng, H. Lin, and M. Z. Hasan, Drumhead surface states and topological nodal-line fermions in TiTaSe_2 , *Phys. Rev. B* **93**, 121113(R) (2016).
- [23] Y.-H. Chan, C.-K. Chiu, M. Y. Chou, and A. P. Schnyder, Ca_3P_2 and other topological semimetals with line nodes and drumhead surface states, *Phys. Rev. B* **93**, 205132 (2016).
- [24] B. Singh, S. Mardanya, C. Su, H. Lin, A. Agarwal, and A. Bansil, Spin-orbit coupling driven crossover from a starfruitlike nodal semimetal to Dirac and Weyl semimetal state in CaAuAs , *Phys. Rev. B* **98**, 085122 (2018).
- [25] S.-Y. Xu *et al.*, Discovery of Lorentz-violating type II Weyl fermions in LaAlGe , *Sci. Adv.* **3**, e1603266 (2017).
- [26] T.-R. Chang, I. Pletikosic, T. Kong, G. Bian, A. Huang, J. Denlinger, S. K. Kushwaha, B. Sinkovic, H.-T. Jeng, T. Valla, W. Xie, and R. J. Cava, Realization of a type-II nodal-line semimetal in Mg_3Bi_2 , *Adv. Sci.* **6**, 1800897 (2019).
- [27] B. Wang, B. Singh, B. Ghosh, W.-C. Chiu, M. M. Hosen, Q. Zhang, L. Ying, M. Neupane, A. Agarwal, H. Lin, and A. Bansil, Topological crystalline insulator state with type-II Dirac fermions in transition metal dipnictides, *Phys. Rev. B* **100**, 205118 (2019).
- [28] F.-Y. Li, X. Luo, X. Dai, Y. Yu, F. Zhang, and G. Chen, Hybrid Weyl semimetal, *Phys. Rev. B* **94**, 121105(R) (2016).
- [29] X. Zhang, Z.-M. Yu, Y. Lu, X.-L. Sheng, H. Y. Yang, and S. A. Yang, Hybrid nodal loop metal: Unconventional magnetoresistance and material realization, *Phys. Rev. B* **97**, 125143 (2018).
- [30] Y. Shao, A. N. Rudenko, J. Hu, Z. Sun, Y. Zhu, S. Moon, A. J. Millis, S. Yuan, A. I. Lichtenstein, D. Smirnov, Z. Q. Mao, M. I. Katsnelson, and D. N. Basov, Electronic correlations in nodal-line semimetals, *Nat. Phys.* **16**, 636 (2020).
- [31] L. Kou, C. Chen, and S. C. Smith, Phosphorene: Fabrication, properties, and applications, *J. Phys. Chem. Lett.* **6**, 2794 (2015).
- [32] F. Xia, H. Wang, J. C. M. Hwang, A. H. C. Neto, and L. Yang, Black phosphorus and its isoelectronic materials, *Nat. Rev. Phys.* **1**, 306 (2019).
- [33] J. Qiao, X. Kong, Z.-X. Hu, F. Yang, and W. Ji, High-mobility transport anisotropy and linear dichroism in few-layer black phosphorus, *Nat. Commun.* **5**, 4475 (2014).
- [34] F. Xia, H. Wang, and Y. Jia, Rediscovering black phosphorus as an anisotropic layered material for optoelectronics and electronics, *Nat. Commun.* **5**, 4458 (2014).
- [35] X. Li, L. Tao, Z. Chen, H. Fang, X. Li, X. Wang, J.-B. Xu, and H. Zhu, Graphene and related two-dimensional materials: Structure-property relationships for electronics and optoelectronics, *Appl. Phys. Rev.* **4**, 021306 (2017).
- [36] Z. J. Xiang, G. J. Ye, C. Shang, B. Lei, N. Z. Wang, K. S. Yang, D. Y. Liu, F. B. Meng, X. G. Luo, L. J. Zou, Z. Sun, Y. Zhang, and X. H. Chen, Pressure-induced electronic transition in black phosphorus, *Phys. Rev. Lett.* **115**, 186403 (2015).
- [37] J. Kim, S. S. Baik, S. H. Ryu, Y. Sohn, S. Park, B.-G. Park, J. Denlinger, Y. Yi, H. J. Choi, and K. S. Kim, Observation of tunable band gap and anisotropic Dirac semimetal state in black phosphorus, *Science* **349**, 723 (2015).
- [38] Y. Liu, Z. Qiu, A. Carvalho, Y. Bao, H. Xu, S. J. R. Tan, W. Liu, A. H. Castro Neto, K. P. Loh, and J. Lu, Gate-tunable giant stark effect in few-layer black phosphorus, *Nano Lett.* **17**, 1970 (2017).
- [39] B. Ghosh, B. Singh, R. Prasad, and A. Agarwal, Electric-field tunable dirac semimetal state in phosphorene thin films, *Phys. Rev. B* **94**, 205426 (2016).
- [40] V. Christiansson, F. Petocchi, and P. Werner, Superconductivity in black phosphorus and the role of dynamical screening, *Phys. Rev. B* **105**, 174513 (2022).
- [41] N. Gong, C. Deng, L. Wu, B. Wan, Z. Wang, Z. Li, H. Gou, and F. Gao, Structural diversity and electronic properties of 3D transition metal tetraphosphides, TMP_4 ($\text{TM} = \text{V, Cr, Mn, and Fe}$), *Inorg. Chem.* **57**, 9385 (2018).
- [42] J. Sun, H.-W. Lee, M. Pasta, H. Yuan, G. Zheng, Y. Sun, Y. Li, and Y. Cui, A phosphorene-graphene hybrid material as a high-capacity anode for sodium-ion batteries, *Nat. Nanotechnol.* **10**, 980 (2015).
- [43] Y. Cheng, Y. Zhu, Y. Han, Z. Liu, B. Yang, A. Nie, W. Huang, R. Shahbazian-Yassar, and F. Mashayek, Sodium-induced reordering of atomic stacks in black phosphorus, *Chem. Mater.* **29**, 1350 (2017).
- [44] W. Jeitschko and P. C. Donohue, The high pressure synthesis, crystal structure, and properties of CrP_4 and MoP_4 , *Acta Cryst.* **B28**, 1893 (1972).
- [45] A. H. Mayo, J. A. Richards, H. Takahashi, and S. Ishiwata, High-pressure synthesis of a massive and non-symmorphic dirac semimetal candidate MoP_4 , *J. Phys. Soc. Jpn.* **90**, 123704 (2021).
- [46] N. Kinomura, K. Terao, S. Kikkawa, and M. Koizumi, Preparation and properties of WP_4 , *J. Solid State Chem.* **48**, 306 (1983).

- [47] M. R. Khan, K. Bu, J.-S. Chai, and J.-T. Wang, Novel electronic properties of monoclinic MP_4 ($M = \text{Cr, Mo, W}$) compounds with or without topological nodal line, *Sci. Rep.* **10**, 11502 (2020).
- [48] P. Hohenberg and W. Kohn, Inhomogeneous electron gas, *Phys. Rev.* **136**, B864 (1964).
- [49] P. E. Blöchl, Projector augmented-wave method, *Phys. Rev. B* **50**, 17953 (1994).
- [50] G. Kresse and J. Furthmüller, Efficient iterative schemes for *ab initio* total-energy calculations using a plane-wave basis set, *Phys. Rev. B* **54**, 11169 (1996).
- [51] G. Kresse and D. Joubert, From ultrasoft pseudopotentials to the projector augmented-wave method, *Phys. Rev. B* **59**, 1758 (1999).
- [52] J. P. Perdew, K. Burke, and M. Ernzerhof, Generalized gradient approximation made simple, *Phys. Rev. Lett.* **77**, 3865 (1996).
- [53] A. A. Mostofi, J. R. Yates, G. Pizzi, Y.-S. Lee, I. Souza, D. Vanderbilt, and N. Marzari, An updated version of wannier90: A tool for obtaining maximally-localised Wannier functions, *Comput. Phys. Commun.* **185**, 2309 (2014).
- [54] Q. Wu, S. Zhang, H.-F. Song, M. Troyer, and A. A. Soluyanov, Wannertools: An open-source software package for novel topological materials, *Comput. Phys. Commun.* **224**, 405 (2018).
- [55] See Supplemental Material at <http://link.aps.org/supplemental/10.1103/PhysRevB.108.235136> for the band structure and topological state with spin-orbit coupling and the robustness of the effective mass anisotropy and hybrid nodal-line state in MP_4 materials.
- [56] C.-X. Liu, X.-L. Qi, H. J. Zhang, X. Dai, Z. Fang, and S.-C. Zhang, Model Hamiltonian for topological insulators, *Phys. Rev. B* **82**, 045122 (2010).
- [57] J. Heyd, G. E. Scuseria, and M. Ernzerhof, Hybrid functionals based on a screened Coulomb potential, *J. Chem. Phys.* **118**, 8207 (2003).